Journal of The Electrochemical Society, **163** (7) A1359-A1368 (2016)
0013-4651/2016/163(7)/A1359/10/$33.00 © The Electrochemical Society

Electronic and Bonding Properties of $LiMn_2O_4$ Spinel with Different Surface Orientations and Doping Elements and Their Effects on Manganese Dissolution

Yoon Koo Lee, Jonghyun Park,[a] and Wei Lu[z]

Department of Mechanical Engineering, University of Michigan, Ann Arbor, Michigan 48109, USA

This paper investigates the effects of surface orientation and doping on the dissolution of Mn ions from $LiMn_2O_4$ structures using first principles calculations. Our aim is to understand why certain surface orientations and element dopings produce structures with lower Mn dissolution. By comparing the electronic properties and structures of systems with different surfaces and dopings, Mn dissolution mechanisms and their prevention can be better understood. Based on our calculations, Mn dissolution is strongly correlated with the electronic and bonding properties of the Mn-O bonds. Surface orientations with a larger number of Mn-O bonds and smaller bond length require more energy to break the Mn-O bonds. In addition, doping with certain elements changes the bonding state of Mn, which either prevents or aggravates Mn dissolution.

Manuscript submitted December 8, 2015; revised manuscript received April 12, 2016. Published April 26, 2016.

Rechargeable batteries using lithium intercalation compounds as the cathode have been extensively studied during the past decade. However, lithium intercalation compounds exhibit significant capacity fading, especially during long-term cycling or storage at elevated temperatures.[1–4] One of the key mechanisms of Li-ion battery degradation involves transition metal dissolution from the cathode materials.[5,6] Among the various lithium intercalation compounds based upon transition metals, which include Mn, Ni, Co, Fe, and Zn, those based upon manganese showed the largest amount of metal ion dissolution.[7] Substantial efforts have been made to understand manganese dissolution mechanisms and further improve battery performance.

Manganese dissolution is an interfacial reaction between the electrode and the electrolyte that relies, to a large extent, upon the surface structures and orientations of the materials. To understand the mechanisms of manganese dissolution, it is essential to understand the reactions taking place at the electrode-electrolyte interface. These reactions depend on the stability, structures, and changes in energy at the electrode surface. Accordingly, surface properties and processes of the electrode have been widely studied using both experimental and computational techniques. For instance, the faceting of solid-state reacted $LiMn_2O_4$ powder particles with different orientations was experimentally investigated.[8] TEM analysis showed that (111) planes possess the lowest surface energy among the low-index surface planes. First-principles calculations have been also used to study surface properties of $LiMn_2O_4$ spinel. Benedek et al. investigated the surface energies and oxidation states of $LiMn_2O_4$ spinels with low index surface structures.[9] Karim et al. revisited the calculation of surface properties and found that the (111) surface is the most stable facet by creating a partial inverse spinel arrangement.[10] In addition to surface stability, different surface orientations of the electrode have been shown to have an effect on Mn dissolution.[11] Spinel with the (111) plane exposed to the electrolyte solution suffers significantly less degradation than spinel with the (110) plane exposed to the electrolyte solution.[11] However, a clear explanation of the impact of surface orientation on manganese dissolution is still missing from previous studies. Investigating the impact of surface orientation on Mn dissolution will broaden our understanding of Mn dissolution.

Preventing or minimizing manganese dissolution is important to improve the performance of this material. Doping with elements that can substitute for manganese ions is known to be an effective way to prevent manganese dissolution. Various metals, such as Al, Co, Cr, Cu, Fe, Mg, and Ni,[12–24] were partially substituted for manganese to prevent the dissolution of manganese. Previous studies have found that the introduction of cations with low oxidation number increases the oxidation state of Mn ions.[25–27] When the oxidation number of the Mn ions in the $LiMn_2O_4$ spinel increases, the overall concentration of Mn^{3+} ions decreases. This phenomenon seems to prevent the Jahn-Teller distortion and disproportionation reactions of unstable Mn^{3+} ions by reducing the concentration of Mn^{3+} ions; this eventually reduces Mn dissolution. Techniques like this have significant success when all of the Mn on the cathode surface is tetravalent.[28] Alternatively, one can also create a nonstoichiometric spinel in which Mn ions are replaced by Li (i.e. $Li_{1+\delta}Mn_{2-\delta}O_4$). This has the same effect of increasing the overall Mn valence. This method has also been shown to increase stability in the higher voltage region.[29] However, doping with other metal ions, such as Y^{3+},[30,31] showed behavior that was the opposite of that seen with other elements. Although doping with yttrium can electrochemically activate manganese to increase its specific capacity, it also promotes dissolution of manganese into the electrolyte.[30] Apparently, doping the structure with elements of low oxidation number is not the only technique that can be used to decrease Mn dissolution. Kim et al. claimed that Mn dissolution is also strongly correlated with the covalent nature of the Mn-O bond.[32] To further understand why doping with certain elements decreases manganese dissolution, a detailed analysis of the electrode's electronic properties in the presence of different doping elements should be investigated.

In summary, this research investigates the effect of surface orientation and doping on the dissolution of Mn ions from $LiMn_2O_4$ structures using first-principles calculations. The aim of our research is to understand why certain surface orientations and element dopings more effectively prevent manganese dissolution. By calculating the electronic and bonding properties of electrodes with different surfaces and dopings, manganese dissolution mechanisms and their prevention can be more fully understood. Specifically, this study conducts a thorough investigation of the changes in surface stability, manganese oxidation state, enthalpy of formation (EOF) of manganese vacancies, electronic properties and bonding properties of electrodes with different surface orientations and element dopings. The calculation results are then validated and compared with previous calculations and experimental results.

Computational Procedure

First-principles electronic structure calculations were performed within the generalized gradient approximation (Perdew-Wang 91 parameterization of the exchange correlation potential) plus U (GGA +U) implementation of density functional theory. The Vienna ab initio simulation package[33] plane-wave pseudopotential code was used with the projected augmented wave (PAW) method. A plane-wave cutoff energy of 600 eV was used in this study to ensure good convergence during cell parameter relaxations. A U value of 4.84 eV was chosen for the Mn atoms, which was the average value of Mn^{3+} (4.64 eV) and Mn^{4+} (5.04 eV). A cell containing eight formula units of $LiMn_2O_4$ was used for the bulk calculations with $8 \times 8 \times 8$ k-point sampling of

[a]Present Address: Department of Mechanical and Aerospace Engineering, Missouri University of Science and Technology, Rolla, Missouri 65409, USA
[z]E-mail: weilu@umich.edu

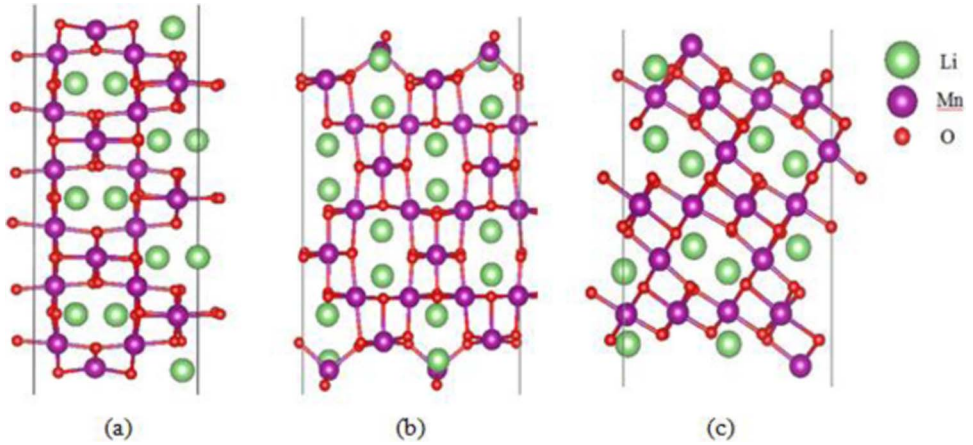

Figure 1. Surface structures of (a) (110) $LiMnO_2$, (b) (001) Mn_4O_8 and (c) (111) Mn.

the Monkhorst-Pack scheme. All our calculations were ensured with a total system energy convergence within 5 meV per atomic unit.

Surface structure of $LiMn_2O_4$.—Benedek et al.[9] adopted low-index surface terminations to simulate the surface structure in their $LiMn_2O_4$ model. In this study, a similar approach was used to create a $LiMn_2O_4$ surface structure model. Three $LiMn_2O_4$ surface models with different orientations [(001), (110) and (111)] were constructed. Given the variety of terminations that are possible, we only considered the common features of $LiMn_2O_4$ surfaces with low index numbers. Within each orientation of the surface, different terminations of atoms on the surface are also possible.

The (110) orientation of the $LiMn_2O_4$ structure has 2 different planes, which consist of a MnO_2 slab and a $LiMnO_2$ slab, occupied in turn. Therefore, two different terminations are available in the (110) orientation. The energy required to break the bond from each MnO_2 and $LiMnO_2$ termination should be different because they have different atoms and because bonds are present near them. When $LiMnO_2$ slabs are placed at both the top and the bottom layers of the slab structure with the (110) orientation, this structure is defined as (110)_$LiMnO_2$ surface structure as shown in Fig. 1a. The sequence of the (110)_$LiMnO_2$ structure can be described as

$$(C_v)\,LiMnO_2,\ MnO_2,\ LiMnO_2,\ \ldots,\ MnO_2,\ (1-C_v)\,LiMnO_2$$

The vacancy concentration, C_v, of the top and the bottom layers were fixed to 0.5 for all the surface structures.[9] The (110)_MnO_2 surface structure has the same sequence as the (110)_$LiMnO_2$ structure, except that both the top and the bottom layers are MnO_2 slabs.

Similarly, we adopted Mn_4O_8 and Li_2 terminations in the (001) orientation. Figure 1b shows the surface structure of (001)_Mn_4O_8. The sequence of (001)_Mn_4O_8 can be described as

$$(C_v)\,Mn_4O_8,\ Li_2,\ Mn_4O_8,\ \ldots,\ Li_2,\ (1-C_v)\,Mn_4O_8$$

The vacancy concentration is also fixed to 0.5 for both (001)_Mn_4O_8 and (001)_Li_2 surface structures.

The surface structures of (111) orientation are slightly more complicated compared to the previous structures. The sequence of the (111)_Mn structure shown in Fig. 1c is

$$(C_v)\,Mn,\ Li,\ O_4,\ Mn_3,\ O_4,\ Li,\ Mn,\ Li,\ \ldots,\ O_4,$$
$$Mn_3,\ O_4,\ Li,\ (1-C_v)\,Mn$$

Mn, Mn_3 and O_4 terminations in the (111) orientation were chosen. In order to make integral numbers of Mn atoms at both the top and the bottom layers of (111)_Mn and (111)_Mn_3 structures, the number of stacking in the supercell parallel to the cleavage surface was doubled.

By considering different surface atom terminations, a total of 7 $LiMn_2O_4$ surface slab models were built in this study. Ideal stoichiometry was maintained by transferring atoms from one surface of the slab to the opposite surface. A vacuum slab was placed on both sides of the $LiMn_2O_4$ slab structure for relaxation. The total thickness of the slab varied slightly due to the cleavage of different orientations and different positions of surface atoms, ranging from 34.2 Å to 36.7 Å after relaxation. Vacuum slabs with a thickness of 10 Å each were placed above and below the structure.

In addition to different surface orientations and terminations, the ferromagnetic (FM) and antiferromagnetic (AFM) orderings of manganese atoms were considered. There are two possible magnetic orderings to achieve anti-ferromagnetism within the spinel manganese oxides:[34] AFM ordering with (001) and (110) directions. The AFM arrangement with (110) direction was adopted in this work because it has been reported that AFM ordering with (110) direction has slightly lower energy than AFM ordering with (001) direction.

Element (Co, Cu, Cr, Fe, Mg Ni and Sn) doping of $LiMn_2O_4$.—Figure 2 shows the element-doped $LiMn_2O_4$ structure with (001) surface orientation. Doping elements (Co, Cu, Cr, Fe, Mg, Ni and Sn) replaced Mn atoms between other two Mn atoms. The changes in electronic and bonding properties of the Mn atoms were investigated by placing different doping elements. The $LiM_{0.5}Mn_{1.5}O_4$ stoichiometry of the doped structure was maintained. In order to compare the effects of different doping elements on the structures, we fixed the doping concentration to 25%, which was a value used by many experiments.[12,14,15,35,36] In this study, changes in average intercalation voltage, oxidation state of manganese, and bonding properties due to doping with different elements (Co, Cu, Cr, Fe, Mg, Ni and Sn) were investigated using first-principles calculations. Based on previous reports, U values for Co, Cu, Cr, Fe, and Ni were 4.0, 5.2, 3.5, 4.2, and 6.4 eV.[37–39]

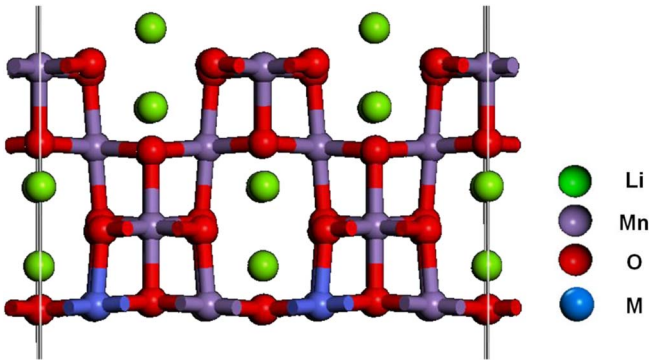

Figure 2. Element (M = Co, Cu, Cr, Fe, Mg, Ni and Sn)-doped $LiMn_2O_4$ structure with (001) surface orientation.

Table I. Surface energy of various surface structures of $LiMn_2O_4$.

Surface structure	Surface energy of ferromagnetic ordering (J/m^2)	Literature value: surface energy for ferromagnetic ordering[9,10] (J/m^2)	Surface energy of antiferromagnetic ordering (J/m^2)
(001)_Li_2	0.554	0.58, 0.87	0.601
(001)_Mn_4O_8	1.199	0.98,1.28	1.229
(110)_$LiMnO_2$	1.233	0.99,1.39	1.248
(110)_MnO_2	1.162	1.19,1.52	1.155
(111)_Mn	0.834	0.85,N/A	0.898
(111)_Mn_3	1.682	1.29,1.18	1.625
(111)_O_4	1.201	1.30,N/A	1.537

Results and Discussion

Surface energy change with different orientations.—The surface energy quantifies the breakdown energy of molecular bonds in the cleaved materials. The surface energy can be defined as the additional energy when surfaces are newly generated compared with that of the bulk material. Surface structures with smaller surface energies are more stable. Thus, the relative stabilities of surfaces with different orientations and structures can be obtained by comparing the differences in their surface energies. The surface energy, σ, can be computed as

$$\sigma = \frac{E_{slab} - N E_{bulk}}{2A} \quad [1]$$

where E_{slab} is the energy of the slab with surfaces on the top and bottom, E_{bulk} is the bulk energy per formula unit, N is the number of chemical formula unis in the slab, and A is the cleavage area of the slab. Here the cleavage area refers to the base area of a slab structure calculated after cleavage and relaxation. The bulk energy refers to the energy of 1 formula unit of $LiMn_2O_4$ supercell, which is −46.75 eV.

The surface energies of different orientations/terminations of the $LiMn_2O_4$ slab model were calculated using Equation 1. Table I shows the surface energies of different orientations and terminations in both the FM and AFM slab structures after relaxation. The surface energy of the each slab structure can be used as a measure of its relative stability, which determines the probable form of structures within the same orientation. For example, lithium terminations in the (001) structure will be a more likely structure than manganese or oxygen terminations because its surface energy is critically lower than that of the other terminations. Among the 7 different surface terminations and orientations, the surface structures of (001)_Li_2, (110)_M_4O_8, and (111)_Mn have the smallest surface energy within the same orientations for both FM and AFM structures.

The surface energies of different surface structures are similar to those reported in the literature,[9] except for the (111)_Mn_3 structure, as shown in Table I. The surface energy of the (111)_Mn_3 structure is quite different compared with those of the other structures. Discrepancies between the literature values and the results of our calculation of the (111) surface energy probably come from the surface reconstruction that occurs during relaxations. Our calculations show an intensive reconstruction of the (111) surface during relaxations. These results are consistent with previous findings that Mn-terminated (111) surfaces experience surface reconstruction during relaxations.[9,10] Benedek et al.[9] found that the Mn-terminated (111) surface structures undergoes extensive migration of Li and O atom from the bulk to the surface, as well as stoichiometric mixing of the Li, Mn and O components. Karim et al.[10] also studied the reconstruction of (111) orientations with relatively high surface energy; they claimed that reconstruction is an indication of the inherent instability of the (111) surface. Karim et al.[10] also found that the (111) surface becomes more stable when employing local cation inversion at the (111) surface. In this work, surface reconstructions were also found in (111) surfaces with relatively high surface energy. However, the surface energy is higher than those from previous reports displayed in Table I. Due to intensive reconstruction, the final relaxation structures and their corresponding energy states might be changed during relaxations. Smearing methods, width of smearing, and other computational methods may influence the final relaxation structures and their corresponding energy states.

The surface energies of $LiMn_2O_4$ structures with FM and AFM ordering are also similar, except for surface structures with (111) orientations. The reconstruction of (111) surfaces results in surface energies for surfaces with FM ordering that are different than those of surfaces with AFM ordering, after relaxation. The spin configuration of the surface structure may influence the surface energy of each of the terminations and orientations, which results in differences in surface energy between FM and AFM structures.

Changes in the manganese vacancy formation energy with different orientations.—The manganese vacancy formation energies were calculated using the $LiMn_2O_4$ surface slab model with different orientations/terminations. Different terminations of the $LiMn_2O_4$ structure have different atoms present on the surface. The energy required to break a bond from each termination should be different because they have different numbers of atoms and bonds are present near them. The energy needed for manganese atoms to break free from the structure can be calculated using the manganese vacancy formation energy, as described in Equation 2:

$$E_F = \frac{1}{M}\left(E[Li_N Mn_{2N-M} O_{4N}] - E[(LiMn_2O_4)_N]\right) + \mu_{Mn}, \quad [2]$$

where E_F is the manganese vacancy formation energy, N is the number of chemical formula units in the system, M is the manganese deficiency number and μ_{Mn} is the chemical potential of manganese. Mn has been widely used as a reference for Mn oxides as well as other transition metals. However, the chemical potential is affected by the specific value of the U parameter.[40] Hoang adopted Hubbard U value as 4.84 eV and also calculated the chemical potential of Mn in the Li-Mn-O phase. The average value of chemical potential of Mn at 0 K in the stable region of the Li-Mn-O phase was about −4.5 eV.[41] In this study, we adopted this value for the calculations. In order to calculate the minimum energy caused by the vacancy of manganese atom, the nearest Mn atom was terminated.

The formation energies and electronic structures of defects in oxygen-deficient $LiMn_2O_4$ were previously investigated to determine the preferred defect types in $LiMn_2O_4$ structures.[42] Simple oxygen vacancies in the $LiMn_2O_4$ structure were found to exhibit the lowest formation energy among the oxygen-vacancy-type defects. Simple oxygen vacancy in the structure refers that the nearest atoms were not moved to fill the vacant space when an oxygen atom was terminated from the structure. Similarly, the formation energies of simple Mn vacancies in $LiMn_2O_4$ with different surface structures were investigated in this study.

By comparing the manganese vacancy formation energies of different surface orientations, the orientation/termination that is more likely to contribute to manganese dissolution by a breaking bond from the structure can be determined. Table II shows the manganese vacancy

Table II. Formation energy of manganese vacancy in various surface structures of $LiMn_2O_4$.

Surface structure	Formation energy of manganese vacancy with ferromagnetic ordering (eV)	Formation energy of manganese vacancy with antiferromagnetic ordering (eV)
(001)_Li_2	10.513	9.506
(001)_Mn_4O_8	9.007	5.733
(110)_$LiMnO_2$	7.547	4.685
(110)_MnO_2	2.112	0.661
(111)_Mn	4.078	3.79
(111)_Mn_3	3.554	4.662
(111)_O_4	6.065	6.685

Table III. $LiMn_2O_4$ surfaces with ferromagnetic ordering.

Surface structure	Number of Mn-O bonds	Average Mn-O bond length (A)	Formation energy of Mn vacancy (eV)	Electrostatic energy (eV)	Change in electrostatic energy (eV)
(001)_Li_2	5	1.879	10.513	27.371	13.334
(001)_Mn_4O_8	4	1.679	9.007	25.583	11.546
(110)_$LiMnO_2$	4	2.002	7.547	21.341	7.304
(110)_MnO_2	3	1.960	2.112	16.642	2.604
(111)_Mn	3	2.192	4.078	14.037	0 (reference)
(111)_Mn_3	3	1.868	3.554	17.189	3.152
(111)_O_4	4	2.344	6.065	17.496	3.459

formation energies of $LiMn_2O_4$ with AFM and FM ordering having different surface structures. To compare the manganese vacancy formation energies within different orientations, the surface structures with the smallest surface energy within each orientation was chosen. From previous surface energy calculations, the surface structures of (001)_Li_2, (110)_MnO_2, and (111)_Mn have the smallest surface energy in their orientations for both FM and AFM structure among the 7 different surface terminations and orientations.

Among FM surface structures, the manganese vacancy formation energies of (001)_Li_2, (110)_MnO_2, and (111)_Mn are 10.5 eV, 2.11 eV and 4.08 eV, respectively. Among AFM surface structures, the manganese vacancy formation energies of (001)_Li_2, (110)_MnO_2, and (111)_Mn are 9.51 eV, 0.66 eV and 3.79 eV, respectively. Among the three different orientations, the manganese vacancy formation energies of surface structures with FM ordering are similar to those with AFM ordering. The (110) surface orientation has the smallest manganese vacancy formation energy, whereas the (001) surface has the largest. This result is consistent with the previous TEM results[11] that $LiMn_2O_4$ with the (111) plane exposed to the electrolyte suffers significantly less degradation than $LiMn_2O_4$ with the (110) plane exposed to the electrolyte.

Changes of bond length and electrostatic energy resulting from different surface orientations.—To understand why certain orientations have smaller dissolution effects and smaller manganese vacancy formation energies, the bonding properties among different surface orientation/terminations were investigated. The ionic character was estimated from the electrostatic interaction between Mn and O. The electrostatic interaction was estimated using the effective charge of each atom[32] and the bond length of Mn-O bonds. The total charge of each atom was obtained from an integration of the charge density in the atomic sphere. The electrostatic energy E_{es} stored in a system of N charges $q_1,q_2,\ldots,q_n$ at positions $r_1,r_2,\ldots,r_n$ can be defined as

$$E_{es} = \frac{1}{2}\sum_{i=1}^{N} q_i \sum_{j=1}^{N(j\neq i)} k_e \frac{q_i}{r_{ij}}, \qquad [3]$$

where r_{ij} is the distance between positions r_i and r_j, and k_e is Coulomb's constant. A value of $k_e = 8.987551\ \mathrm{N\ m^2/C^2}$ was used. Mn ions on the surface and the nearby O ions were chosen to calculate the electrostatic energy of Mn-O bonds with different surface structures.

The number of Mn-O bonds near the manganese atom and the bond lengths of Mn-O bonds change with surface orientations and terminations of the structure. In general, the length and strength of the bond are inversely proportional with each other. If bond length decreases, the energy required to break the bond increases. Moreover, if there are additional bonds near the atom, the energy required to break the Mn-O bond also increases. There are different numbers of bonds near the manganese atoms with different terminations and orientations among $LiMn_2O_4$ samples with different surface structures. Moreover, the bond lengths near the manganese atom are uniquely determined by the atom's surroundings and the structure during relaxation. Thus, the number of Mn-O bonds and their bond lengths will be uniquely determined by the surface orientation/terminations. The number of Mn-O bonds, the average Mn-O bond length, the manganese vacancy formation energy of surfaces, the electrostatic energy of Mn-O bonds, and the change in electrostatic energy with FM and AFM ordering can be found in Table III and Table IV, respectively.

To understand the relationship among manganese vacancy formation energy, bond length, and the number of Mn-O bonds near the manganese atoms in the surface structures, these properties are plotted separately. Figure 3 shows the relationship among manganese vacancy formation energy, bond length and the number of Mn-O bonds near the manganese atoms in the surface structures with FM and AFM ordering, respectively. At a glance, it seems that there is no conspicuous relationship among the number of bonds, bond length and manganese vacancy formation energy. However, a larger number of Mn-O bonds correlates with higher manganese vacancy formation energy. Now we compare the relationship between manganese vacancy formation energy and bond length in cases containing the same number of bonds in Fig. 3a. For example, the (001)_Li_2 structure has the highest manganese vacancy formation energy, since the manganese atom has five Mn-O bonds in its vicinity. Surface structures with 4 Mn-O bonds near the manganese atom have smaller manganese vacancy formation energies than surface structures with 5 Mn-O bonds, but higher manganese vacancy formation energies than structures with 3 Mn-O bonds. Among the surface structures with 4 Mn-O bonds, the average bond length near the Mn atom is inversely proportional to the manganese vacancy formation energy. The (111)_Mn_3 structure is an outlier among the surface structures. If it followed the trend, it should have either a larger bond length or smaller manganese vacancy formation energy. The reason for this result comes mainly from surface reconstruction that occurs during relaxation of the (111) structure. Without this exception, the manganese vacancy formation energy seems to be determined by the number of bonds near the manganese atom and the bond length of each of the Mn-O bonds.

Table IV. $LiMn_2O_4$ surfaces with anti-ferromagnetic ordering.

Surface structure	Number of Mn-O bonds	Mn-O bond length (A)	Energy of Mn vacancy (eV)	Electrostatic energy (eV)	Change in electrostatic energy (eV)
(001)_Li_2	5	1.869	9.506	26.976	12.217
(001)_Mn_4O_8	4	1.667	5.733	24.563	9.804
(110)_$LiMnO_2$	4	2.008	4.685	20.785	6.026
(110)_MnO_2	3	2.225	0.661	14.262	−0.497
(111)_Mn	3	2.048	3.79	14.759	0 (reference)
(111)_Mn_3	3	1.660	4.662	18.758	3.999
(111)_O_4	4	2.114	6.685	19.151	4.392

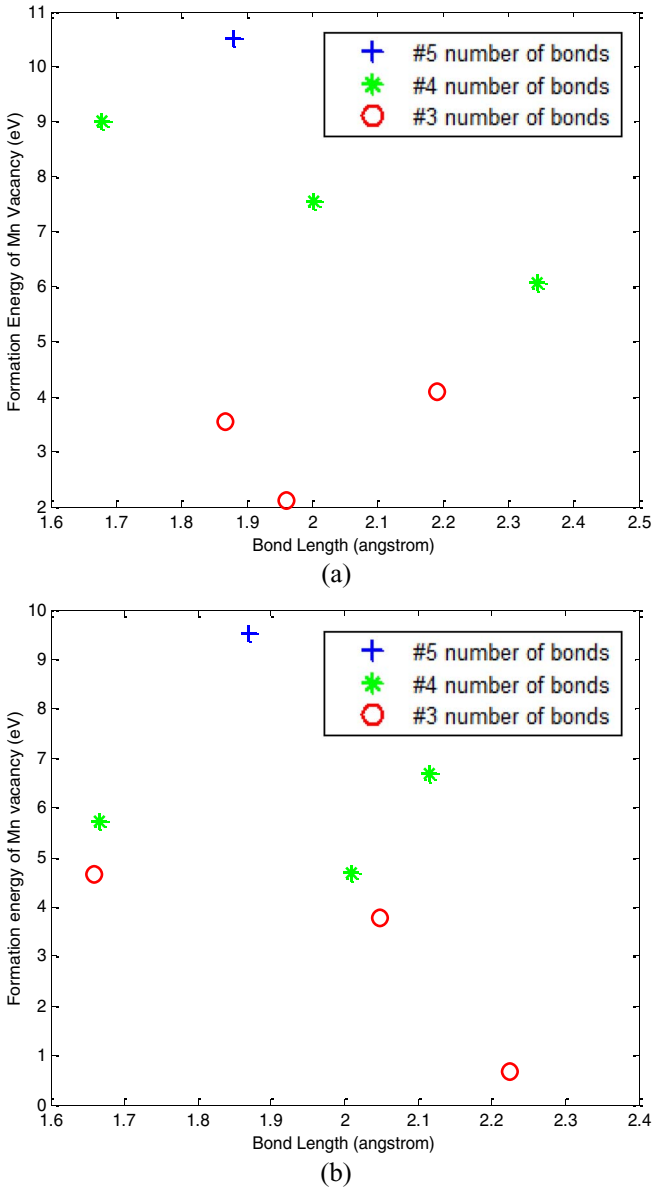

Figure 3. Relationship among the number of Mn-O bonds, average Mn-O bond length and manganese vacancy formation energy of surfaces with (a) ferromagnetic ordering, and (b) anti-ferromagnetic ordering.

AFM surface structures show a similar trend with different numbers of bonds. Those structures with a larger number of Mn-O bonds near the surface have higher manganese vacancy formation energies, as shown in Fig. 3b. However, the relationship between the bond length and the manganese vacancy formation energy is not as clear as that seen with the FM structures. This is due to the different spin configurations of nearby Mn atoms. The differences in spin configuration affect the Mn-O bond length, which affects the manganese vacancy formation energy. From these results, it can be concluded that the formation energy of manganese vacancy changes with different surface orientations and that this change is caused by differing numbers of Mn-O bonds near the Mn atom and the bond length of each bond.

The electrostatic energy of Mn-O bonds in various surface structures is also an indicator that elucidates the bonding strength. The electrostatic attraction was calculated using the bond length of Mn-O bonds and the effective charge of each atom[32] shown in Table V. Figure 4 shows the comparison of formation energy of Mn vacancy and change in electrostatic energy of Mn-O bonds in 7 different $LiMn_2O_4$ surface structures with respect to the (111)_Mn structure with ferromagnetic and anti-ferromagnetic ordering. The trend shows that the electrostatic energy and the formation energy of manganese vacancy are roughly proportional to each other. These results further highlight the importance of the number of Mn-O bonds and their bonding properties on different surfaces.

Table V. Effective charge of Mn and O ions in $LiMn_2O_4$ surfaces with ferromagnetic and anti-ferromagnetic ordering.

	FM		AFM	
Surface structure	Effective charge of Mn	Average value of effective charge of O	Effective charge of Mn	Average value of effective charge of O
(001)_Li_2	1.427	−0.9902	1.408	−0.9838
(001)_Mn_4O_8	1.123	−1.03375	1.054	−0.99875
(110)_$LiMnO_2$	1.441	−1.02825	1.194	−1.018
(110)_MnO_2	1.386	−1.04667	1.366	−1.032
(111)_Mn	1.508	−0.98733	1.5	−0.983
(111)_Mn_3	1.552	−1.03033	1.51	−1.01267
(111)_O_4	1.401	−0.98	1.388	−0.97867

DOS distribution with different orientations.—To understand the effect of surface orientation on manganese dissolution, first-principles calculation methods were used to calculate the electronic properties of the surfaces. Previous studies have reported that the oxidation state of the manganese ions influences manganese dissolution.[25–27,32] The oxidation state of manganese is closely related to the number of electrons in the d-orbitals, which consist of the e_g and t_{2g} orbitals. The e_g orbital consists of the d_{x2-y2} and d_{z2} orbitals and the t_{2g} orbital consists of the d_{xy}, $d_{xz,}$ and d_{yz} orbitals. Generally, it is assumed that only 3 electrons inhabit the t_{2g} level in the electronic configuration of an ideal high-spin Mn^{4+} ion. The electronic configuration of an ideal high-spin Mn^{3+} ion is assumed to have only 3 electrons in the t_{2g} orbital and one electron in the e_g orbital. If only one electron is placed in the e_g orbital, that electron is placed in either the d_{x2-y2} or the d_{z2} orbital. Due to the presence of the electron, the degeneracy of the two orbitals breaks down, decreasing the geometric stability and leading to Jahn-Teller distortion. Due to this instability, avoiding the Mn^{3+} state of manganese prevents Jahn-teller distortion, resulting in reduced Mn dissolution.[25–27]

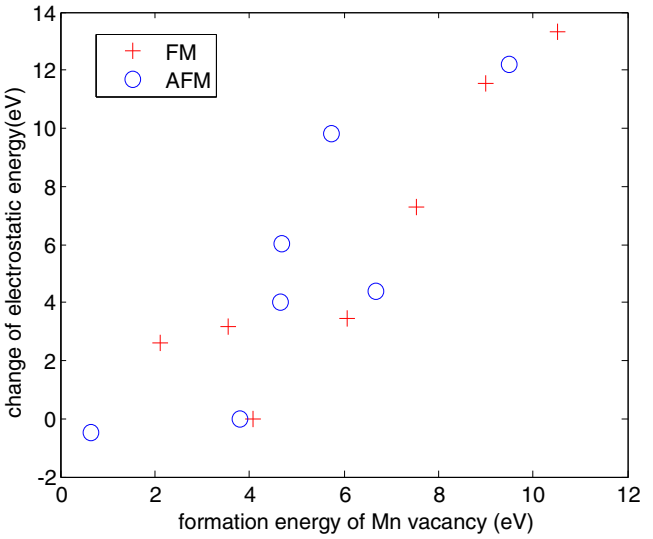

Figure 4. Comparison of formation energy of Mn vacancy and change in electrostatic energy of Mn-O bonds in 7 different $LiMn_2O_4$ surface structures with respect to the (111) _ Mn structure with ferromagnetic (FM) and anti-ferromagnetic (AFM) ordering.

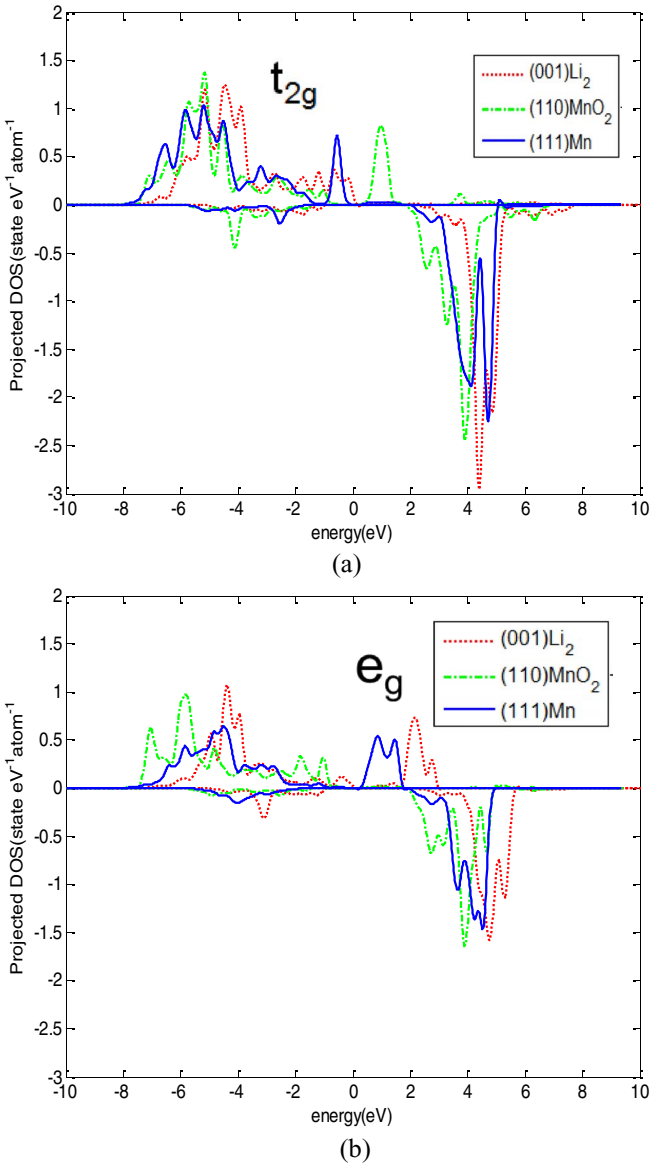

Figure 5. Comparison of (a) t_{2g} and (b) e_g orbitals in Mn projected DOS among (001)_Li_2, (110)_MnO_2, and (111)_Mn surface structures.

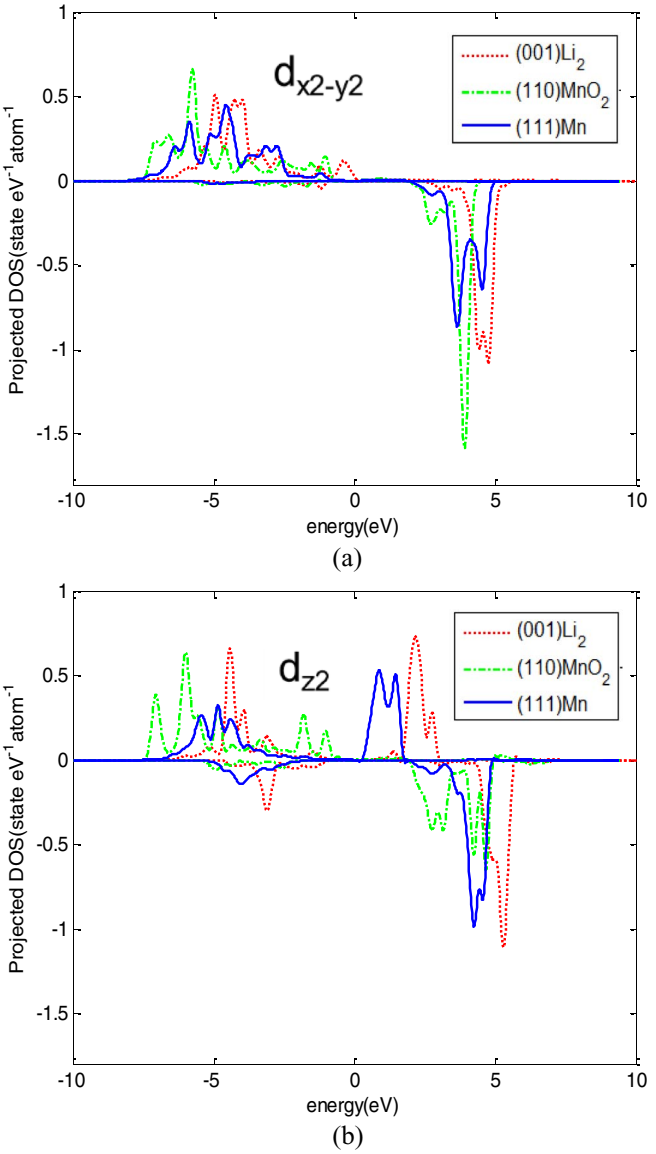

Figure 6. Comparisons of the (a) d_{x2-y2} and (b) d_{z2} states in the e_g orbital in the Mn projected DOSs among (001)_Li_2, (110)_MnO_2, and (111)_Mn surface structures.

To observe the electronic properties and the oxidation state of the manganese atom, the projected density of state (DOS) of a manganese atom on the surface was investigated. Comparisons of the projected DOSs of Mn atoms in (001)_Li_2, (110)_MnO_2, and (111)_Mn surface structures can be found in Fig. 5 and Fig. 6. The "+" and "−" signs in these figures indicate the up and down spin directions of the manganese atoms. Since the oxidation state of the manganese is determined by the d-orbital state with highest energy, only energy changes from −10 to +10 eV are extracted.

Figure 5a compares the complete t_{2g} orbitals of the manganese atoms on the surfaces of three different surface structures. From these results, it can be seen that the up-spin t_{2g} level is fully filled with electrons because it is below the Fermi energy level. Since the t_{2g} orbitals are completely filled with electrons whether the manganese atom has an oxidation number of 3 or 4, the t_{2g} orbitals of different surface structures are not significantly different among them. However, the e_g orbitals from the three different surface structures show different patterns than the t_{2g} orbitals, as shown in Fig. 5b. The DOS of the high state e_g orbitals in the up-spin have splits near the Fermi level with different surface structures. The (001)_Li_2 structure has a peak at the highest energy state (near 3 eV) and the (110)_MnO_2 structure has a peak at the lowest energy state (<−1 eV) among the energy peaks. As the energy state of the e_g orbital increases above 0 eV, it will become harder to fill the e_g orbital with electrons. This means that increasing the energy state of the e_g orbital increases the possibility of the existence of a Mn^{4+} state, which will be beneficial for preventing Mn dissolution.

To further investigate the state of the e_g orbital, the DOSs of the d_{x2-y2} and d_{z2} orbitals are plotted separately. Figure 6 shows the projected DOSs of the d_{x2-y2} and d_{z2} orbitals of the manganese atom. Some changes in the energy level can be observed among the d_{x2-y2} and d_{z2} orbitals in different surface structures, which mainly come from Jahn-Teller distortions. When a molecule possesses a degenerate electronic ground state, it will distort its structure to remove degeneracy and form a lower energy state. Elongation and compression are two ways to remove the degeneracy. When elongation occurs in the z direction, the axial bond length increases and degeneracy is broken by the stabilization of the d orbitals with a z component. The energies of the d orbitals with a z component (d_{z2}) decrease while the energies of the d orbitals without a z component (d_{x2-y2}) increase. On the other hand,

when compression occurs in the z direction, the axial bond length decreases and the degeneracy is broken by the stabilization of d orbitals without a z component. The energies of d orbitals without a z component (d_{x2-y2}) decrease while the energies of d orbitals with a z component (d_{z2}) increase. From the results of our calculations, it can be anticipated that different surface structures of $LiMn_2O_4$ experience different degree of Jahn-teller distortion. (110)_MnO_2 surface structure has the lowest energy level in the dz_2 state, which probably has been elongated mostly in the z direction, whereas (001)_Li_2 structure has the highest energy level in the dz_2 state, which has the shortest axial bond.

The changes in the DOS peak energy state are different among the three different structures. The (001)_Li_2 structure shows a DOS peak at a higher energy state in the up-spin state. In contrast, the (110)_MnO_2 structure has a DOS peak at the lowest energy state in the up-spin state, as shown in Fig. 6a. The relative position of the Mn 3d levels is shifted to a high-energy region in the (001)_Li_2 structure. Since the relative peak position of Mn 3d level in (001)_Li_2 is shifted to the right, above the Fermi level, more energy is needed for an electron to fill the e_g orbital. This implies that more energy is needed to achieve the 3+ oxidation state of manganese. Thus, the (001)_Li_2 surface structure has the lowest possibility to be in the 3+ oxidation state and the (110)_MnO_2 structure has the highest possibility to be in the 3+ oxidation state. These results agree with previous calculations of the manganese vacancy formation energy, which indicate that the (110) orientation is the most vulnerable and the (001) orientation is the least vulnerable to Mn dissolution.

Element (Co, Cu, Cr, Fe, Mg, Ni and Sn) doping of $LiMn_2O_4$.— Doping with various elements influences the phase stability, redox potential, ionic and electronic conductivity of the Li-Mn-O structure. From previous reports, Co, Cu, Cr, Fe, Mg, Ni and Sn doping were thermodynamically stable in Li-Mn-O phase structures.[12,14–20,35,36,40,43–45] Also, dopants greatly change Li diffusion of the Li-Mn-O structures. Due to charge balance and opening of diffusion channel, some of the Li-site dopants acted as activation centers, facilitating the diffusion of neighboring Li ions.[43,46] The influence of dopants on charge conductivity was also reported in the previous literature[41,43,47–50] which differs depending on different dopants. Our main focus in this work is to understand why certain dopants are more effective in preventing manganese dissolution. In doing so, redox potential was calculated and compared with previous reports to validate our calculation of the structures. Electronic structures and bonding properties of Mn-O bonds were investigated to understand the cause of Mn dissolution.

To validate the results of our calculations of the structures of element-doped $LiMn_2O_4$, the average intercalation voltages were calculated after doping with different elements. The average intercalation voltage was calculated from changes in the Gibbs free energy of lithiated and delithiated $LiMn_2O_4$ structures, as shown in equation 4:

$$V = -\frac{E[(LiMn_2O_4)_N] - E[Li_{N-Z}(Mn_2O_4)_N] - E(Li_Z)}{ZF}, \quad [4]$$

where Z is the amount of lithium extracted from the structure and F is Faraday constant. The total energies of the fully lithiated and de-lithiated structures were calculated, and then the average intercalation voltages were predicted. Table VI. shows the average intercalation voltages for the $LiM_{0.5}Mn_{1.5}O_4$ to $M_{0.5}Mn_{1.5}O_4$ transition (M = Mn, Co, Cr, Cu, Fe, Mg, Ni and Sn) taken from References 12,14–20,35,36,44,45, from experiments[12,14,15,35,36] and from the calculations performed in this work. The results clearly show that the values calculated in this work are within the range of those in the references and similar to those taken from experimental results. Since it is more beneficial to operate a battery in the higher voltage region, most doping elements, except for Sn, were favorable in terms of intercalation voltage.

DOS distribution with different doping elements.— To observe the effect of doping on the electronic properties of $LiMn_2O_4$ structures, the total DOS was investigated after doping with different elements. Figure 7a shows the total DOS of $LiMn_2O_4$ with and without Co doping. The shape of the total DOS diagram is shifted to higher energy states, especially in the higher energy region. In contrast, the total density of states of $LiMn_2O_4$ with Sn doping and Cr doping are shifted to lower energy states, as shown in Figs. 7b and 7c, respectively. Our calculations of DOS changes with transition metal elements are consistent with those in the literature,[17,18] which also showed that doping with transition metal elements changes the overall energy state of the DOS. Our results are also similar to those of previous reports,[17,18] which found that the electronegativity of the transition metal ion affects the changes in DOS.

Table VI. Average intercalation voltages from $LiM_{0.5}Mn_{1.5}O_4$ to $M_{0.5}Mn_{1.5}O_4$ (M = Mn, Co, Cr, Cu, Fe, Mg, Ni and Sn) taken from references, experiments and the values calculated in this study.

Doping elements	Reference	Experiment results	Calculations in this work
without doping	3.78∼4.05 V[12,14,16,17,19,44]	4 V[12]	4.01
Co	3.9∼4.2 V[17,35]	4.2 V[35]	4.06
Cr	4.04∼4.5 V[17,19,20,45]	4.5 V[14]	4.11
Cu	4.15∼4.56 V[14,18,20]	4.45 V[14]	4.50
Fe	3.8∼4.28 V[17,19,36]	4 V[36]	4.24
Ni	4.12∼4.8 V[14,15,17]	4.35 V[15]	4.25
Mg	N/A	N/A	4.79
Sn	N/A	N/A	3.82

To investigate changes in the oxidation state and electronic properties of Mn ions in the $LiMn_2O_4$ structure, the e_g orbital in the projected DOSs of Mn atoms with different doping elements were investigated. Figure 8a compares the e_g orbital in the projected DOSs of Mn atoms in $LiMn_2O_4$ with Cr doping, Cu doping, or without doping. It can be seen that doping with elemental Cu shifted the overall DOS of the Mn atom to a higher energy level. As seen with the effects of orientation, a shift to the higher energy region makes it more difficult to fill the orbitals with electrons to create Mn^{3+} ions in the structure. This means that doping with Cu is an effective way to increase the oxidation state of manganese. However, doping with Cr shows the opposite behavior, compared with Cu doping, in the DOS state. Figure 8a shows that doping with Cr shifts the overall DOS of the Mn atom to a lower energy level. Projecting the DOS of the Mn atom in the Cr-doped structure gave results that were opposite of the predictions that doping with metals of low oxidation number will increase the overall energy state to higher level. It seems that the electronegativity of the transition metal element might be more related to the DOS of the Mn atom than the oxidation number of the doping element. Doping with a transition metal element of higher electronegativity shows larger energy shift in the projected DOS of the Mn atom.

Figure 8b shows the comparisons between projected DOS of the Mn atom in the $LiMn_2O_4$ structure with Mg doping, Sn doping, or without doping. Figure 8b shows that doping with either Mg or Sn increases the up-spin state below the Fermi level, whereas doping decreases the down-spin state above the Fermi level. These two DOSs of the Mn atom in the Mg and Sn-doped structures do not show different trends, even though Mg and Sn have different oxidation numbers. Similarly, the DOS state of the Mn ion may not be directly related to the oxidation states of these two elements.

COHP (Crystal Orbital Hamiltonian Population) analysis.— To further expand our understanding of the electronic and bonding properties of Mn, the COHP (Crystal Orbital Hamiltonian Population) of Mn in structures with different dopings were investigated. A COHP diagram gives information regarding bonding, anti-bonding, and non-bonding energy regions within a specified energy range. COHP divides the band-structure energy into the sum of orbital interactions.[51–53] If there are bonding contributions, the system energy is lowered, and

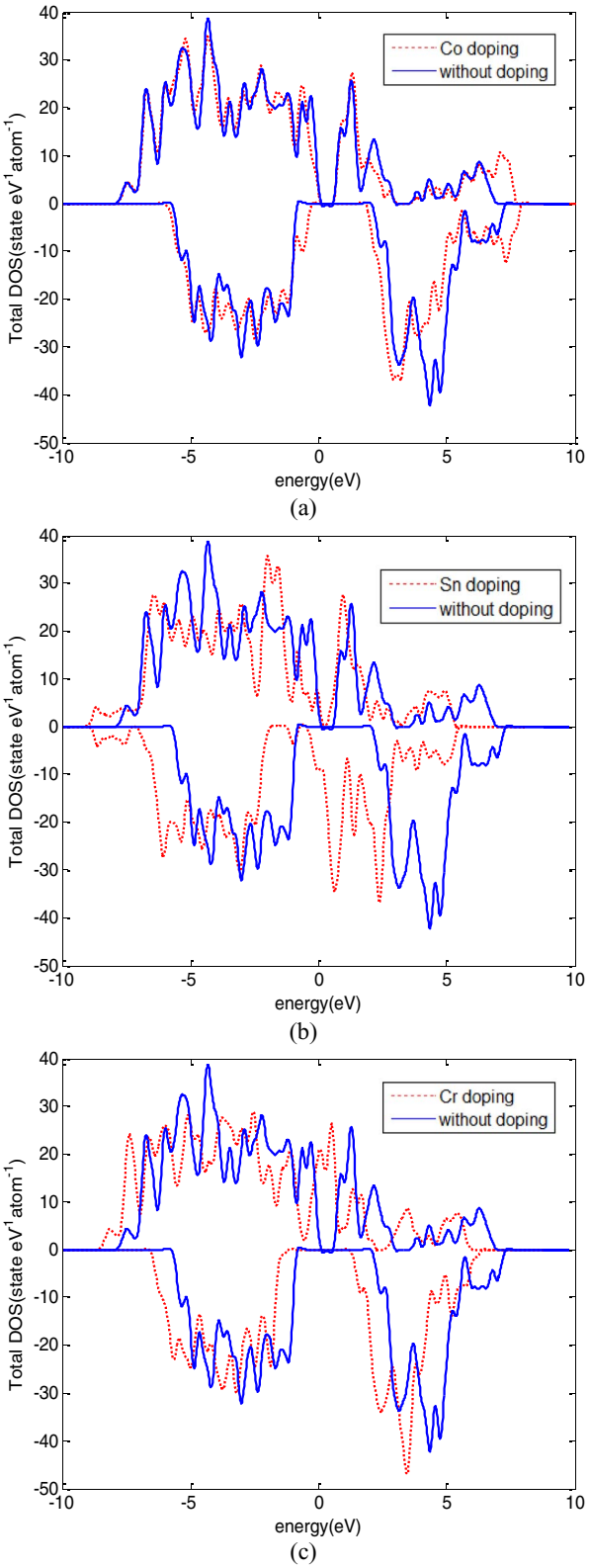

Figure 7. Total DOS of $LiMn_2O_4$ structures with (a) Co doping (b) Sn doping (c) Cr doping.

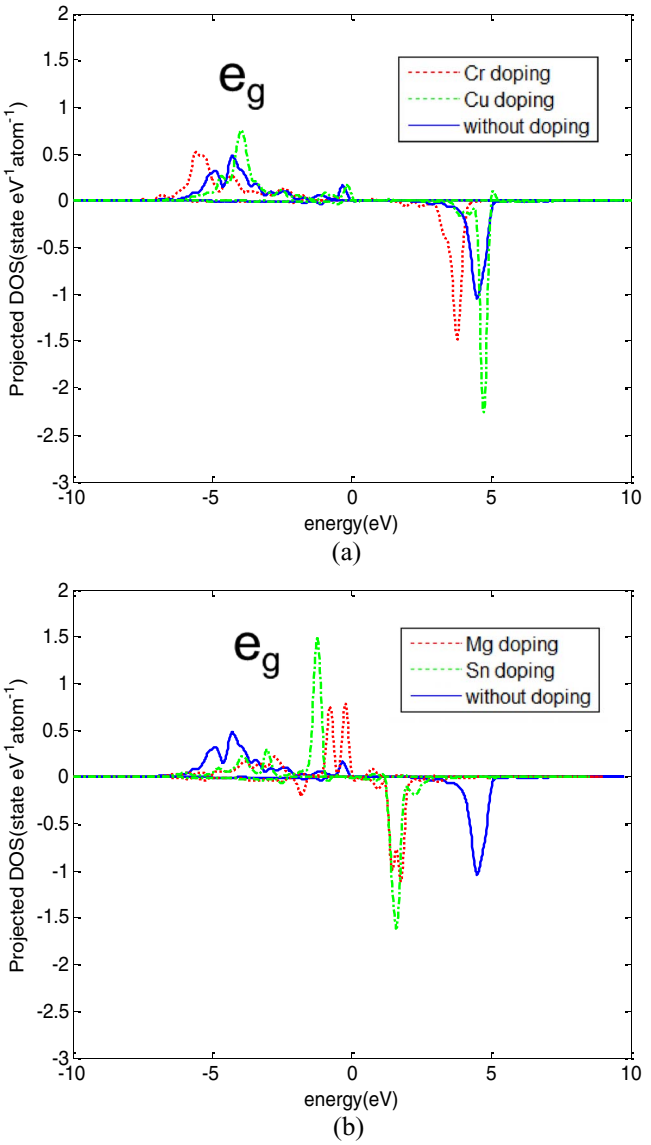

Figure 8. The e_g orbital in the projected DOS of the Mn atom in $LiMn_2O_4$ structures with (a) Cr doping, Cu doping, and without doping, and (b) Mg doping, Sn doping, and without doping.

the COHP has a negative value. Conversely, if there are anti-bonding contributions, the COHP has a positive value. Figure 9 compares the COHP diagram of the manganese atom in a $LiMn_2O_4$ structure without doping to those doped with Cu, Sn, or Mg. The x-axis of the diagram indicates the negative value of the COHP. This means that values in the figure that are >0 indicate a bonding state and negative values of –COHP indicate an anti-bonding state of the Mn atom. The zero energy state of the diagram is adjusted to the Fermi energy.

When we compare the bonding state below the Fermi level (when all the electrons are filled in the atom), the Mn atom with Cu doping shows more bonding state and less anti-bonding state than the Mn atom without doping, as shown in Fig. 9a. This result is the exact opposite of the results displayed by the Mn atom with Sn doping, which shows less bonding state and more anti-bonding state of the Mn atom, as shown in Fig. 9b. A state showing more covalent bonding and less anti-bonding increases the covalency of the Mn-O bonds, which reduces Mn dissolution. At higher temperatures, a number of electrons become activated over the Fermi level. A sharp peak of positive (anti-bonding) COHP appears in the lower energy above the Fermi level in the Mn atom with Sn doping. If an anti-bonding state dominates above the Fermi level, electronic instability is expected to be increased. However, the positive peak (anti-bonding) of the COHP decreases in the Mn atom with Cu doping. This result indicates that doping with Sn is likely to decrease stability at higher temperature, which will aggravate Mn dissolution.

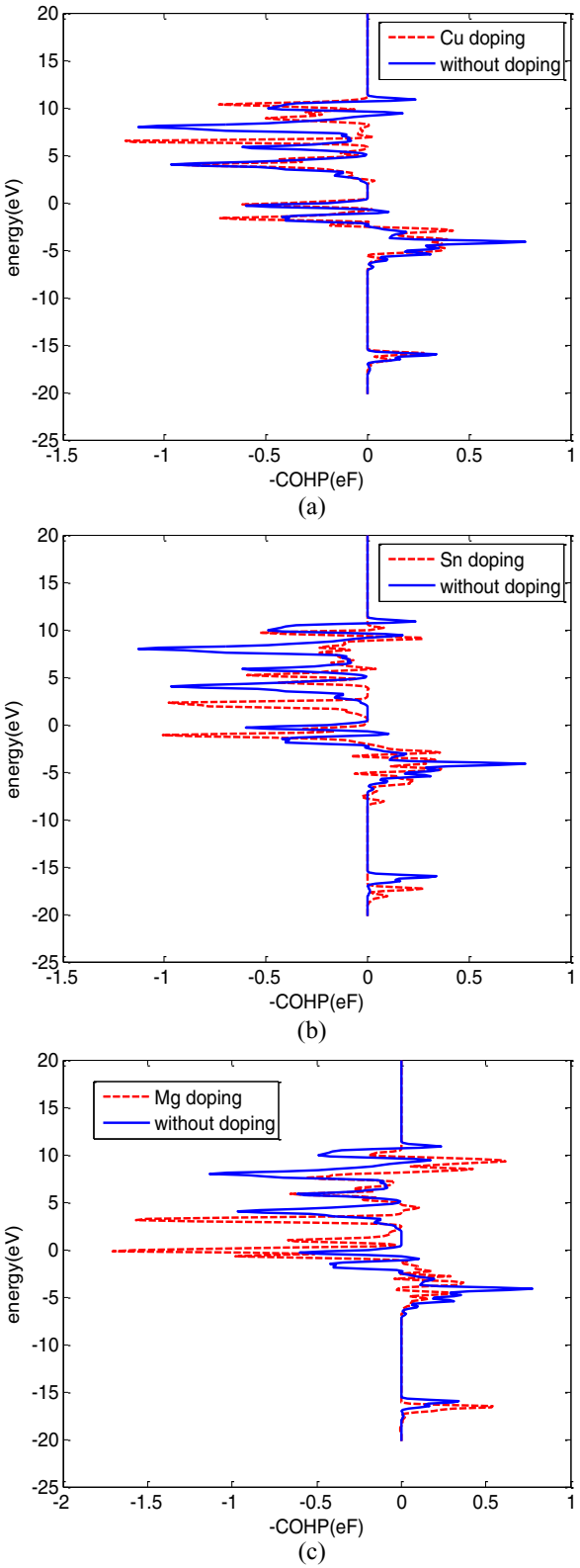

Figure 9. COHP diagrams of Mn atoms in $LiMn_2O_4$ with (a)Cu, (b)Sn and (c)Mg doping.

Doping with Mg ions results in a state with more covalent bonding and less anti-bonding, as shown in Fig. 9c. Although the overall energy state is decreased after doping with Mg, as seen with Sn doping, there are more COHP in the stable energy state (low energy state near −20 eV) than without doping. These results also indicate that doping with Mg is beneficial for preventing Mn dissolution.

Table VII. Integration of COHP in $LiMn_2O_4$ and its change after doping with different elements.

Doping element	Integration of COHP (eF)	Change (%)
without doping	−1.3089	0
Co	−1.53937	17.6079
Cr	−1.36651	4.401401
Cu	−1.31086	0.1497
Fe	−1.40853	7.6117
Mg	−2.18478	66.9173
Ni	−1.59129	21.5746
Sn	−1.06316	−18.7745

To compare the bonding characteristics with different doping elements numerically, total integrations of the COHPs with different doping elements were performed. Table VII shows the values of the total integrals of the COHPs with different dopings, with respect to the energy where all the electrons are filled in the manganese atom. Energy integration of the COHP represents the contribution of a chemical bond to the distribution of specific atom energies.[51] These results show that doping with Co, Cr, Cu, Fe, Mg and Ni increases the bonding state of the Mn-O bond. However, doping with Sn increases the anti-bonding state. These results are consistent with experimental results from the literature, which showed that doping with Sn increases Mn dissolution whereas doping with other elements decreases Mn dissolution. From the COHP analysis, element doping is beneficial to increase the Mn-O bonding state in the order of Mg, Ni, Co, Fe, Cr and Cu below the Fermi energy level. However, these elements also affect the oxidation state of Mn in the $LiMn_2O_4$ structure at higher temperature. For instance, Mg-doped $LiMn_2O_4$ structure has more Mn^{3+} oxidation states at higher temperature because the DOS of e_g orbital above Fermi energy will decrease to the lower energy region. Although Mg doping will increase the bonding state of Mn-O bonds, high temperature will increase the Mn^{3+} oxidation state which will increase the instability of the structure.

It should be noted that in this paper we considered the dissolution of Mn in $LiMn_2O_4$ in vacuum. While a slab model in vacuum is commonly used in various DFT studies, it has its limitations. A more rigorous calculation will need to consider the impact of electrolyte, which may affect the dissolution behavior. On the other hand, Mn dissolution is mainly caused by the dissociation of Mn–O bonds followed by the diffusion of Mn ions to the environment regardless of the reaction routes in the $LiMn_2O_4$ structure. Therefore, the local electronic and bonding properties of Mn ions and the bonds with nearest oxygen ions obtained in this paper can still provide useful information of Mn dissolution by comparing various $LiMn_2O_4$ surface structures.

Conclusions

The effect of surface orientations and doping on the dissolution of Mn ions from $LiMn_2O_4$ structures was investigated using first principles calculations. Specifically, the changes in surface stability, manganese oxidation state, manganese vacancy EOF, electronic properties and bonding properties with different surface orientations and element doping were examined. To validate the model of the surface structures and doped structures of $LiMn_2O_4$, their surface energy and average intercalation voltage were compared with the results of several previous studies.

Based on our results, surface orientations with a larger number of Mn-O bonds and smaller bond length require more energy to break the Mn-O bonds. The Mn vacancy formation energies showed that increasing energy is needed to break the Mn-O bond in the order of (110), (111) and (001) surface orientations. These results agree with the projected DOS of the Mn atom, which showed that the (001) surface has the lowest possibility to be in the 3+ oxidation state and

the (110) surface has the highest possibility to be in the 3+ oxidation state.

Changes in the electronic and bonding properties of Mn atoms due to different doping elements were investigated. Within the transition metal elements, a DOS analysis showed that the Mn projected DOS is more related to the electronegativity of the doping element than to the oxidation state of the doping element. However, doping with Mg and Sn does not show the specific trend with respect to changes in the Mn DOS. To further investigate the electronic and bonding properties of the Mn atoms, a COHP analysis was conducted with different doping elements. Doping with Co, Cr, Cu, Fe, Mg and Ni increases the bonding state of the Mn-O bond, whereas doping with Sn decreases the bonding state. These results are consistent with the experimental results from previous literature, which showed that doping with Sn increases Mn dissolution whereas doping with other elements decreases Mn dissolution. From the COHP analysis, element doping is beneficial to increase the Mn-O bonding state in the order of Mg, Ni, Co, Fe, Cr and Cu below the Fermi energy level. However, these elements also affect the oxidation state of Mn in the $LiMn_2O_4$ structure at higher temperature. In order to the understand the overall transition metal dissolution, both the bonding state and oxidation state should be considered.

In conclusion, Mn dissolution from $LiMn_2O_4$ structures is strongly correlated with the electronic properties and bonding properties of the Mn-O bonds. It is important to understand the properties of these Mn-O bonds to prevent Mn dissolution. In addition, avoiding unstable Mn^{3+} is important to prevent Jahn-teller distortions and disproportionation reactions at higher energy states of the structure. These results indicate that first-principles calculations can provide important guidance to select surface orientations and doping elements to prevent Mn dissolution.

Acknowledgments

This research was funded by the GM/UM Advanced Battery Coalition for Drivetrains. Support from our sponsor is gratefully acknowledged.

References

1. P. Arora, R. E. White, and M. Doyle, *Journal of The Electrochemical Society*, **145**, 3647 (1998).
2. Y. Dai, L. Cai, and R. E. White, *Journal of The Electrochemical Society*, **160**, A182 (2013).
3. D. Zhang, B. S. Haran, A. Durairajan, R. E. White, Y. Podrazhansky, and B. N. Popov, *Journal of Power Sources*, **91**, 122 (2000).
4. J. Vetter, P. Novak, M. R. Wagner, C. Veit, K. C. Möller, J. O. Besenhard, M. Winter, M. Wohlfahrt-Mehrens, C. Vogler, and A. Hammouche, *Journal of power sources*, **147**, 269 (2005).
5. J. Shim, R. Kostecki, T. Richardson, X. Song, and K. A. Striebel, *Journal of Power Sources*, **112**, 222 (2002).
6. L. Yang, M. Takahashi, and B. Wang, *Electrochimica Acta*, **51**, 3228 (2006).
7. W. Choi and A. Manthiram, *Journal of The Electrochemical Society*, **153**, A1760 (2006).
8. M.-R. Huang, C.-W. Lin, and H.-Y. Lu, *Applied Surface Science*, **177**, 103 (2001).
9. R. Benedek and M. M. Thackeray, *Physical Review B*, **83**, 195439 (2011).
10. A. Karim, S. Fosse, and K. A. Persson, *Physical Review B*, **87**, 075322 (2013).
11. M. Hirayama, H. Ido, K. Kim, W. Cho, K. Tamura, J. i. Mizuki, and R. Kanno, *Journal of the American Chemical Society*, **132**, 15268 (2010).
12. R. Koksbang, J. Barker, M. Y. Saïdi, K. West, B. Zachau-Christiansen, and S. Skaarup, *Solid State Ionics*, **83**, 151 (1996).
13. A. Osnis, M. Kosa, D. Aurbach, and D. T. Major, *The Journal of Physical Chemistry C*, **117**, 17919 (2013).
14. B. Xu, Develop high energy high power Li-ion battery cathode materials : a first principles computational study, in *PhD Thesis*, University of California, San Diego (2012).
15. Y. Ein-Eli, J. T. Vaughey, M. M. Thackeray, S. Mukerjee, X. Q. Yang, and J. McBreen, *Journal of the Electrochemical Society*, **146**, 908 (1999).
16. L. Benco, J.-L. Barras, M. Atanasov, C. A. Daul, and E. Deiss, *Solid State Ionics*, **112**, 255 (1998).
17. S. Shi, C. Ouyang, D.-s. Wang, L. Chen, and X. Huang, *Solid State Communications*, **126**, 531 (2003).
18. S. Shi, D.-s. Wang, S. Meng, L. Chen, and X. Huang, *Physical Review B*, **67**, 115130 (2003).
19. Y. Liu, T. Fujiwara, H. Yukawa, and M. Morinaga, *Computational Materials Science*, **22**, 309 (2001).
20. S. H. Buta, A first principles investigation of transitional metal doping in lithium battery cathode materials, in *SM Thesis*, Massachusetts Institute of Technology (1999).
21. M. E. Arroy y de Dompablo and J. Morales, *Journal of The Electrochemical Society*, **153**, A2098 (2006).
22. Y. M. Chiang, D. R. Sadoway, Y. I. Jang, B. Huang, and H. Wang, *Electrochemical and Solid-State Letters*, **2**, 107 (1999).
23. T. Tsuji, M. Nagao, Y. Yamamura, and N. Tien Tai, *Solid State Ionics*, **154–155**, 381 (2002).
24. H. J. Bang, V. S. Donepudi, and J. Prakash, *Electrochimica Acta*, **48**, 443 (2002).
25. D. H. Jang, Y. J. Shin, and S. M. Oh, *Journal of The Electrochemical Society*, **143**, 2204 (1996).
26. D. H. Jang and S. M. Oh, *Journal of The Electrochemical Society*, **144**, 3342 (1997).
27. J. M. Tarascon, E. Wang, F. K. Shokoohi, W. R. McKinnon, and S. Colson, *Journal of The Electrochemical Society*, **138**, 2859 (1991).
28. J.-W. Song, C. C. Nguyen, H. Choi, K.-H. Lee, K.-H. Han, Y.-J. Kim, S. Choy, and S.-W. Song, *Journal of The Electrochemical Society*, **158**, A458 (2011).
29. R. J. Gummow, A. de Kock, and M. M. Thackeray, *Solid State Ionics*, **69**, 59 (1994).
30. X. He, J. Li, Y. Cai, Y. Wang, J. Ying, C. Jiang, and C. Wan, *Journal of Power Sources*, **150**, 216 (2005).
31. X. He, W. Pu, Y. Cai, X. Wang, C. Jiang, and C. Wan, *Acta Chimica Sinica*, **63**, 1853 (2005).
32. Y. Kim, J. Lim, and S. Kang, *International Journal of Quantum Chemistry*, **113**, 148 (2013).
33. R. Benedek, M. M. Thackeray, J. Low, and T. Bučko, *The Journal of Physical Chemistry C*, **116**, 4050 (2012).
34. C. Y. Ouyang, S. Q. Shi, and M. S. Lei, *Journal of Alloys and Compounds*, **474**, 370 (2009).
35. C. H. Shen, R. S. Liu, R. Gundakaram, J. M. Chen, S. M. Huang, J. S. Chen, and C. M. Wang, *Journal of Power Sources*, **102**, 21 (2001).
36. K. Amine, H. Tukamoto, H. Yasuda, and Y. Fujita, *Journal of Power Sources*, **68**, 604 (1997).
37. F. Zhou, M. Cococcioni, C. A. Marianetti, D. Morgan, and G. Ceder, *Physical Review B*, **70**, 235121 (2004).
38. D. O. Scanlon, B. J. Morgan, and G. W. Watson, *The Journal of chemical physics*, **131**, 124703 (2009).
39. G. Hautier, S. P. Ong, A. Jain, C. J. Moore, and G. Ceder, *Physical Review B*, **85**, 155208 (2012).
40. R. C. Longo, F. T. Kong, S. Kc, M. S. Park, J. Yoon, D. H. Yeon, J. H. Park, S. G. Doo, and K. Cho, *Physical Chemistry Chemical Physics*, **16**, 11233 (2014).
41. K. Hoang, *Journal of Materials Chemistry A*, **2**, 18271 (2014).
42. Y. Koyama, I. Tanaka, H. Adachi, Y. Uchimoto, and M. Wakihara, *Journal of The Electrochemical Society*, **150**, A63 (2003).
43. F. Kong, R. C. Longo, M.-S. Park, J. Yoon, D.-H. Yeon, J.-H. Park, W.-H. Wang, K. C. Santosh, S.-G. Doo, and K. Cho, *Journal of Materials Chemistry A*, **3**, 8489 (2015).
44. M. K. Aydinol and G. Ceder, *Journal of The Electrochemical Society*, **144**, 3832 (1997).
45. C. M. Julien and A. Mauger, *Ionics*, **19**, 951 (2013).
46. F. Kong, R. C. Longo, D.-H. Yeon, J. Yoon, J.-H. Park, C. Liang, S. Kc, Y. Zheng, S.-G. Doo, and K. Cho, *The Journal of Physical Chemistry C*, **119**, 21904 (2015).
47. Y. J. Wei, L. Y. Yan, C. Z. Wang, X. G. Xu, F. Wu, and G. Chen, *The Journal of Physical Chemistry B*, **108**, 18547 (2004).
48. T. T. Fang and H. Y. Chung, *Journal of the American Ceramic Society*, **91**, 342 (2008).
49. J. Marzec, K. Świerczek, J. Przewoźnik, J. Molenda, D. R. Simon, E. M. Kelder, and J. Schoonman, *Solid State Ionics*, **146**, 225 (2002).
50. M. Park, X. Zhang, M. Chung, G. B. Less, and A. M. Sastry, *Journal of Power Sources*, **195**, 7904 (2010).
51. R. Dronskowski and P. E. Bloechl, *The Journal of Physical Chemistry*, **97**, 8617 (1993).
52. V. L. Deringer, A. L. Tchougréeff, and R. Dronskowski, *The Journal of Physical Chemistry A*, **115**, 5461 (2011).
53. S. Maintz, V. L. Deringer, A. L. Tchougréeff, and R. Dronskowski, *Journal of computational chemistry*, **34**, 2557 (2013).